

Adapting Vision-Language Foundation Model for Next Generation Medical Ultrasound Image Analysis

Jingguo Qu[†], Xinyang Han[†], Jia Ai, Juan Wu, Tong Zhao, Tonghuan Xiao, Sheng Ning, Yuqi Yang, Jing Qin
Senior Member, IEEE, Ann Dorothy King, Winnie Chiu-Wing Chu, Jing Cai, and Michael Tin-Cheung Ying

Abstract—Vision-Language Models (VLMs) have demonstrated remarkable generalization capabilities, yet their application to medical ultrasound remains constrained by the significant domain shift between natural images and sonographic data. The unique physics of ultrasound, manifesting as speckle noise, shadowing, and variable artifacts, often leads to suboptimal performance when applying off-the-shelf foundation models. To address this, we propose a novel Hybrid-tuning (HT) strategy for the efficient adaptation of CLIP-based models to ultrasound analysis. Our method introduces a lightweight adapter module integrated into the frozen visual backbone, featuring frequency-domain filtering to suppress periodic artifacts and dynamic noise estimation to calibrate feature representations. Furthermore, we design specialized segmentation and classification heads that employ multi-scale feature aggregation to maximize the utility of pre-trained semantic priors. Extensive evaluations across six multi-center datasets (covering lymph nodes, breast, thyroid, and prostate) reveal that our HT-enhanced models significantly outperform existing state-of-the-art methods, including BiomedCLIP and standard LoRA fine-tuning. The results highlight the superior data efficiency and robustness of our approach, paving the way for practical, foundational intelligence in automated ultrasound diagnosis. The source code is available at [GitHub](#).

Index Terms—Foundation model, domain adaptation, fine-tuning, ultrasound, lymph node, breast lesion

I. INTRODUCTION

Ultrasonography (US) is a common medical imaging technique used in clinical practice. It is particularly favored for evaluating superficial structures, including breast lesions [1], thyroid nodules [2], and lymph nodes [3], [4], [5], due to its ability to provide real-time visualization in a noninvasive and cost-effective manner. Utilizing high-frequency ultrasound, US delivers detailed views of internal anatomy and is routinely used in clinical examinations. Currently, radiologists need to manually identify and delineate regions of interest (ROIs) on ultrasound images to diagnose diseases and develop treatment

[†] Equal contribution. This work was supported by General Research Funds of the Research Grant Council of Hong Kong (Reference no. 15102222 and 15102524). (*Corresponding authors: Michael Tin-Cheung Ying*)

Jingguo Qu, Xinyang Han, Tonghuan Xiao, Sheng Ning, Yuqi Yang, Jing Cai, and Michael Tin-Cheung Ying are with the Department of Health Technology and Informatics, The Hong Kong Polytechnic University, Hong Kong, China (e-mail: michael.ying@polyu.edu.hk).

Jing Qin is with the Centre for Smart Health and School of Nursing, The Hong Kong Polytechnic University, Hong Kong, China.

Ann Dorothy King and Winnie Chiu-Wing Chu are with the Department of Imaging and Interventional Radiology, The Chinese University of Hong Kong, Hong Kong, China.

Jia Ai, Juan Wu are with Suzhou Hospital of Traditional Chinese Medicine Affiliated to Nanjing University of Chinese Medicine, Suzhou, China.

Tong Zhao is with the Department of Ultrasound, The Affiliated Changzhou No. 2 People's Hospital of Nanjing Medical University, Changzhou, China.

plans, which is a time-consuming process and subject to variability depending on the experiences of radiologists.

However, the inherent imaging vulnerabilities of ultrasonography poses challenges to this process, including grainy appearance, ill-defined ROI boundaries, low contrast, and the presence of image artifacts. Furthermore, the shapes, sizes, and locations of ROIs can vary substantially across scan planes and patient anatomies. These factors make manual annotation laborious and inconsistent, underscoring the need for automated methods that can reliably detect, segment and classify ROIs to improve diagnostic efficiency and accuracy. Thus, automated ultrasound image analysis is a potential direction for standardized and regulated diagnosis and treatment.

Deep learning has driven significant advances in medical image analysis [6], [7], but these methods rely on large volumes of expertly annotated data [8] and lack generalizability [9]. Foundation models (FMs) [10], which are pre-trained on vast and diverse datasets offer a way to relax this requirement. By capturing broad visual representations during pre-training, they can be efficiently fine-tuned with few labeled ultrasound scans, while still maintaining coherent, task-relevant features. This paradigm holds great promise for more practical, data-efficient analysis in clinical practice. Yet, despite growing interest in adapting FMs to specialized domains, their application to ultrasound image analysis remains under-explored.

Mainstream FMs (CLIP [11], SAM [12], DINOv2 [13]) have shown impressive performance in various computer vision tasks, such as zero-shot classification [11], semantic segmentation [12], [13] and visual-language interactions [14]. Although several studies [15], [16] have investigated the application of FMs in medical ultrasound image analysis, the efficacy of these specialized models, when trained solely on comparatively smaller ultrasound datasets, is still debated against the performance of original FMs pre-trained on extensive natural image datasets [17]. Consequently, the development of domain adaptation techniques for specific downstream domains and tasks based on original FMs remains a promising research direction.

To address this problem, we propose a novel and parameter-efficient framework Hybrid-tuning (HT) to adapt CLIP-based models [11], [18], [19], [20] for medical ultrasound image analysis, which is designed to be seamlessly integrated into the vision transformer backbone of CLIP. Our methodology involves fine-tuning the pre-trained CLIP and its variants on a radiological image-text dataset, where only the lightweight HT module is trained. The resulting adapted model is then evaluated on a comprehensive suite of downstream tasks,

including zero-shot classification, supervised classification, and semantic segmentation on various ultrasound datasets. Datasets include the in-house lymph node ultrasound datasets from two different centers (LN-INT, LN-EXT), the publicly available breast ultrasound image (BUSI) dataset [21], thyroid datasets DDTI [22] and TN3K [23], and microultrasound scans of prostate [24]. Our experimental results demonstrate that this HT technique significantly outperforms baseline methods, establishing a new state-of-the-art for adapting vision-language models to the medical ultrasound domain.

II. RELATED WORK

FMs [10] represent a class of large-scale models pre-trained on vast datasets through self-supervised learning, enabling them to tackle a wide variety of tasks via transfer learning. Prominent examples include GPT [25], SAM [12], BERT [26], CLIP [11] and DINOv2 [13].

Among these, CLIP [11] distinguishes itself with a contrastive pre-training framework that aligns images and text within a shared embedding space by minimizing the cosine distance between correlated image-text pairs. This approach allows CLIP to perform zero-shot classification using text prompts such as “A photo of {class}” without additional re-training. In the medical domain, adaptations like PubMedCLIP [27] and MedCLIP [20] have primarily targeted visual question answering (VQA) tasks. Meanwhile, CLIPSeg [28] builds on this framework by incorporating support images alongside compact text prompts, extending its applicability to binary segmentation during inference time.

Numerous studies have investigated the applications of FMs in medical image analysis. Huix *et al.* [29] evaluated FMs on medical image classification tasks and found that, while these models can outperform state-of-the-art (SOTA) approaches pre-trained on ImageNet [30], their performance varies inconsistently across datasets of different scales, suggesting limitations in robustness and generalizability.

In contrast to leveraging original pre-trained weights, some researchers have pursued training CLIP-like models from scratch using exclusively medical data. PMC-CLIP [31] harnessed approximately one million biomedical image-text pairs from PubMed Central Open Access Subset across 12 modalities, achieving SOTA results in various downstream tasks such as image-text retrieval, image classification and medical VQA. BiomedCLIP [18] further scaled this effort by expanding the closed-source PMC-15M dataset to 15 million pairs. To address the gap of data transparency, UniMedCLIP [19] curated an open-source cross-modal dataset to pre-train a unified vision-language model, which comprising over 5.3 million samples and across six modalities.

Despite the evident importance of the scale of biomedical datasets demonstrated by these studies, the current sizes of curated datasets are significantly smaller than the original CLIP dataset, which consists of approximately 400 million natural image-text pairs. Research such as MetaCLIP [32] has established a clear positive correlation between the scale of datasets and model performance of CLIP and its variants. It is also been reinforced by Poudel *et al.* [17] that large-scale datasets offer advantages unattainable with smaller,

domain-specific collections. Furthermore, most studies in this field primarily concentrated on sparse prediction tasks (*e.g.*, classification), while dense tasks (critical for detailed medical image analysis, *e.g.*, semantic segmentation) are still rarely reported.

Given the persistent challenge of obtaining large-scale, high-quality multi-modal medical datasets, domain adaptation of CLIP models pre-trained on expansive natural datasets emerges as a promising avenue for future research.

III. METHOD

The overall architecture of our method is illustrated in Fig. 1. Firstly, the proposed adapter HT is integrated into the visual branch of frozen CLIP. The curated and cleaned radiological image-text pairs are utilized to facilitate CLIP fine-tuning. Secondly, segmentation and classification heads are attached to the image encoder merged with adapter to perform supervised tasks. Additionally, ensembled prompts are constructed for each disease represented in the ultrasound scans for CLIP zero-shot ability evaluation.

A. Fine-tuning

The present study places particular emphasis on two adapters: LoRA [33] and our proposed Hybrid-tuning (HT) adapter, which is an evolution of Mona [34], as illustrated in Fig. 2.

LoRA [33]. To alleviate the computational burden of full fine-tuning, researchers introduced trainable low-rank matrices into specific layers, typically within the query, key, and value matrices in self-attention mechanism of Transformer. Instead of updating all model parameters, LoRA freezes the original weights and adapts the model via these additional low-rank matrices. This strategy significantly reduces the number of trainable parameters while still achieving performance comparable to fully fine-tuned models.

HT Adapter. While LoRA [33] focuses on specific attention components, we propose a more comprehensive HT adapter, which builds upon the Mona [34] architecture but introduces significant enhancements for medical imaging. Unlike the original Mona developed for Swin-Transformer [35], our HT adapter is tailored for the standard Vision Transformer (ViT) [36] in CLIP and addresses challenges like high-frequency noise and periodic artifacts in medical images. The architecture is illustrated in Fig. 3.

Formally, let $\mathbf{Z} \in \mathbb{R}^{N \times B \times D}$ denote the input sequence. The adapter first projects \mathbf{Z} to a bottleneck dimension d after normalization:

$$\mathbf{Z}_{in} = (\text{LayerNorm}(\mathbf{Z}) \odot \gamma + \mathbf{Z} \odot \gamma_x) \mathbf{W}_{down} + \mathbf{b}_{down} \quad (1)$$

where $\mathbf{W}_{down} \in \mathbb{R}^{D \times d}$, γ and γ_x represent the same weights as Mona [34] for the two parts. \mathbf{Z}_{in} is reshaped into a 2D feature map $\mathbf{F}_{in} \in \mathbb{R}^{B \times d \times H \times W}$.

To suppress global periodic artifacts (*e.g.*, reverberation), we employ a learnable channel-wise filter $\Theta \in \mathbb{R}^d$. \mathbf{F}_{in} is transformed to the frequency domain via 2D FFT, modulated by Θ and reconstructed:

$$\mathbf{F}_{freq} = \text{IFFT2D}(\text{FFT2D}(\mathbf{F}_{in}) \odot \Theta) \quad (2)$$

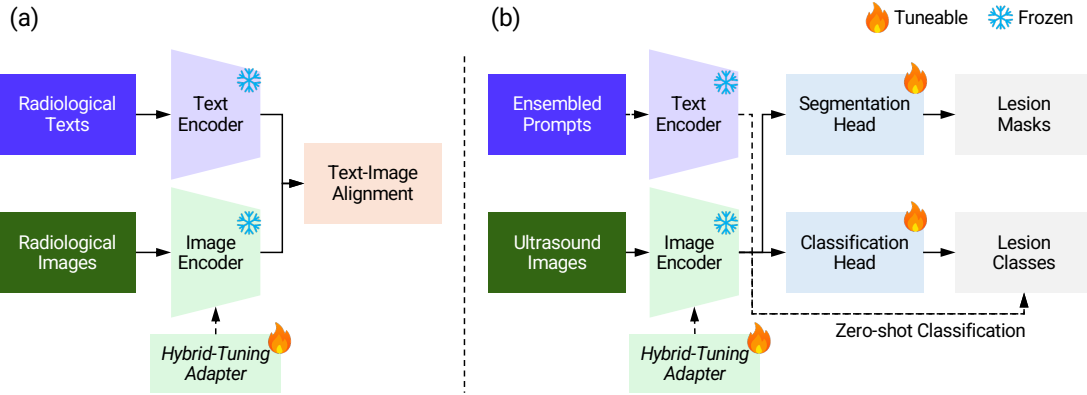


Fig. 1. Overview of proposed workflow. (a) **Fine-tuning stage**. Introduce trainable HT adapter into frozen CLIP to bridge the domain gap between natural images and radiological scans. (b) **Downstream tasks**. Apply trainable heads for ultrasound image segmentation and classification in a supervised manner (solid arrows), and assess zero-shot ultrasound diagnosis capability of CLIP by using ensembled prompt-image pairs (dashed arrows).

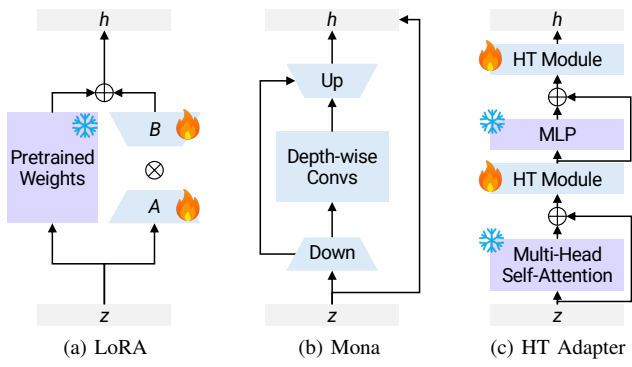


Fig. 2. Structure overview of the original LoRA, Mona and HT adapter based on Mona for CLIP vision encoder (ViT).

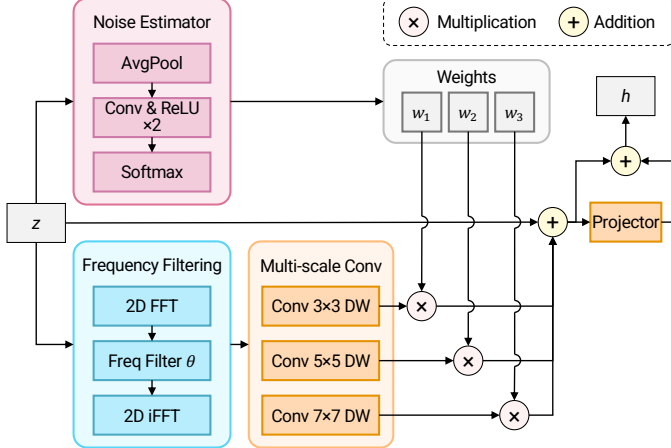


Fig. 3. Architecture of Hybrid-tuning module.

A dynamic multi-scale convolution bank is applied to handle variable noise levels (e.g., speckle noise). A noise estimator computes attention weights $\alpha \in \mathbb{R}^{B \times 3}$ from \mathbf{F}_{freq} using global average pooling (GAP) and an MLP:

$$\alpha = \text{Softmax}(\mathbf{W}_2 \cdot \text{ReLU}(\mathbf{W}_1 \cdot \text{GAP}(\mathbf{F}_{freq}))) \quad (3)$$

Three parallel depth-wise separable convolutions with kernel sizes $k \in \{3, 5, 7\}$ extract spatial features, which are fused

using α :

$$\mathbf{F}_{multi} = \sum_{i=1}^3 \alpha_i \odot \text{DWConv}_{k_i}(\mathbf{F}_{freq}) \quad (4)$$

Finally, residual connections preserve high-frequency details, and the feature map is projected back to the original dimension D to obtain the output \mathbf{H} :

$$\mathbf{H} = \mathbf{Z} + (\text{Dropout}(\text{GELU}(\mathbf{Z}_{out})) \mathbf{W}_{up} + \mathbf{b}_{up}) \quad (5)$$

where \mathbf{Z}_{out} is the reshaped sequence from the processed feature map \mathbf{F}_{multi} . This design allows for seamless integration with pre-trained CLIP weights while effectively handling medical image characteristics.

B. Downstream Tasks

In this study, the downstream tasks comprise lesion segmentation and characteristics classification. To leverage the rich representations from the pre-trained encoder, we implement a multi-scale feature aggregation strategy followed by lightweight task-specific heads.

Multi-level Feature Aggregation. Rather than utilizing only the final embedding and inspired by CLIPSeg [28], we extract feature maps from intermediate Transformer blocks (specifically indices 3, 6, and 9) to capture a hierarchy of visual concepts. Let \mathbf{F}_l denote the feature map from layer l . Each \mathbf{F}_l is projected to a reduced dimension d_{red} and refined through a non-linear block consisting of LayerNorm and linear layers. The processed features are then summed element-wise to yield a unified representation $\mathbf{F}_{agg} \in \mathbb{R}^{B \times d_{red} \times H \times W}$. This approach fuses low-level spatial details with high-level semantics while maintaining computational efficiency.

Segmentation Head. For the segmentation task, we employ a lightweight decoding scheme to generate dense predictions. The unified feature map \mathbf{F}_{agg} is bi-linearly up-sampled to the original image resolution (224×224), followed by a 1×1 convolution that projects features into the label space. This minimalist design circumvents the computational burden of heavy transposed convolutions, ensuring parameter efficiency while delivering precise segmentation masks.

Classification Head. Parallel to segmentation, the classification head extracts global descriptors from \mathbf{F}_{agg} . We apply Adaptive Average Pooling to collapse spatial dimensions, resulting in a compact feature vector. This vector is processed by a MLP consisting of two linear layers with ReLU activation and dropout. Such a structure balances representational capacity with regularization, minimizing the risk of over-fitting on data-scarce medical benchmarks.

IV. EXPERIMENTS

A. Datasets

There are three types of dataset usage in this study, including fine-tuning, segmentation and classification. The overview of datasets and partitions are shown in Table I.

TABLE I

OVERVIEW OF DATASETS AND PARTITIONS. FT., SEG., AND CLS. REFER TO FINE-TUNING, SEGMENTATION AND CLASSIFICATION TASKS, RESPECTIVELY.

Dataset	Training	Validation	Testing	Total	FT.	Seg.	CLS.
PMC-OA [31]	4,942	534	0	5,476	✓		
CURD [37]	13,228	1,500	0	14,728	✓		
MedPix [38]	21,512	2,391	0	23,910	✓		
LN-INT	1,019	127	127	1,273	✓	✓	
LN-EXT	0	0	374	374	✓	✓	
BUSI [21]	518	65	64	647	✓	✓	
DDTI [22]	510	64	63	637	✓		
TN3K [23]	2,304	575	614	3,493	✓		
Prostate [24]	1,937	215	758	2,910	✓		

PMC-OA [31], **CURD** [37] and **MedPix** [38] serve as the primary data sources for fine-tuning process. The original PMC-OA dataset contains 1,848,719 images across various medical imaging modalities. From this collection, ultrasound images and their corresponding captions were extracted, while low-resolution images were excluded. The CURD dataset comprises ultrasound images and captions from 7,390 patients presenting with breast, liver, or thyroid abnormalities. In addition, the MedPix dataset, which comprises 24,485 image-text pairs across CT and MRI imaging modalities, serves to bridge the gap between natural images and medical images, thereby facilitating the fine-tuning process for large models. The Qwen3-8B [39] model was employed to translate captions in CURD dataset into English as they are originally written in Chinese.

During fine-tuning, the raw data underwent a multi-step preprocessing pipeline to ensure quality and consistency. First, we cleaned the textual captions by removing special characters and stripping extraneous whitespace. To provide meaningful descriptive textual content, samples with captions shorter than 20 characters were discarded. Following text cleaning, we removed any entries for which the corresponding image file was not found. Finally the resulting cleaned dataset was then randomly shuffled and partitioned into training and validation sets, using a 9:1 split.

Lymph Node (LN). We collected two LN datasets, **LN-INT** comprises 1,273 ultrasound images (785 benign and 488 malignant) of 307 cases, with years ranging from 2016 to 2024, and **LN-EXT** includes of 374 images (190 benign and 184 malignant). All images are annotated at the pixel level by

experienced radiologists to delineate the LN region. Notably, **LN-EXT** is used exclusively as an external test set and is not involved in any part of the training process.

BUSI [21]. There are 780 breast lesion ultrasound images in BUSI, with 437 benign, 210 malignant and 133 normal cases. The normal cases without ROIs are excluded in the following experiments as the purpose of this study is to detect and segment the abnormal regions.

DDTI [22]. The DDTI dataset consists of 637 ultrasound images of thyroid nodules. The dataset includes a wide range of lesion types including focal thyroiditis, cystic nodules, adenomas and thyroid cancer.

TN3K [23]. The TN3K dataset was collected at Zhujiang Hospital, Southern Medical University. For each patient, only one representative image is retained from those captured at similar viewpoints or anatomical locations. The dataset comprises 2,879 images for training and 614 images for testing.

Prostate [24]. This dataset comprises both expert and non-expert prostate annotations of 75 patients, and only the expert annotations are used in this study.

B. Settings

Implementation Details. Prior to training, to minimize the impact of irrelevant information, non-imaging regions containing overlay annotations are cropped from self-collected ultrasound images. Subsequently, all images are resized to 224×224 pixels for both training and testing. An overview of the datasets and their partitions is provided in Table I. Except for TN3K [23] and Prostate [24], all datasets are randomly divided into training, validation, and test sets in an 8:1:1 ratio. For TN3K and Prostate, the predefined training set is further split into training and validation subsets using an 8:2 ratio, while the original test set remains unchanged.

The whole fine-tuning process lasts for 32 epochs, while the models are trained for 200 epochs for the downstream tasks. The default learning rate for both fine-tuning and downstream tasks was set to 10^{-4} , using a cosine annealing scheduler and a weight decay of 10^{-2} . The loss functions used are InfoNCE loss for fine-tuning, Dice cross-entropy loss for segmentation, and focal loss for classification. All experiments utilize the AdamW optimizer with $\beta_1 = 0.9$ and $\beta_2 = 0.95$, and the batch size is set to 32. All experiments were conducted on a single NVIDIA RTX 4090D GPU with 24 GB memory.

Evaluation Metrics. We used four widely-used metrics to evaluate the segmentation performance of the proposed method: Dice score (Dice, %), intersection over union (IoU, %), 95-percentile of Hausdorff distance (HD95), and average symmetric surface distance (ASD). For classification, Accuracy (Acc, %), Recall (Rec, %), Precision (Pre, %), F1 score (%) and area under receiver operating characteristic curve (AUC, %) are adopted as evaluation metrics. All metrics are calculated based on the binary segmentation and classification results and averaged across all images in the test set.

C. Perquisites

The SOTA CLIP variants used for comparison in this study include raw CLIP [11], BiomedCLIP [18], UniMedCLIP [19],

and MetaCLIP [32]. To establish a visual-only performance baseline, we also evaluate models that rely solely on image input, including UNet [8], ResNet18 [40], and DINOV2 [13]. For all experiments and comparisons, we adopt the ViT-Base architecture with a patch size of 16×16 pixels as the standard backbone. Pre-trained weights are used when publicly available for the respective models.

Given that the zero-shot classification inference process of CLIP [11] necessitates text information as guidance, we devise specialized prompts for the ultrasound image classification task. Instead of adopting generic templates (*e.g.*, “a photo of a [CLASS]”), we construct an ensemble of clinically detailed descriptions for benign and malignant lesions, with each category comprising ten diverse prompts. These prompts capture specific sonographic features such as shape (oval vs. round), margin (circumscribed vs. spiculated), and echogenicity (homogeneous vs. heterogeneous). During inference, we compute the cosine similarity between the image embedding and the ensemble of text embeddings for each class. The final prediction is determined by averaging the similarity scores across all prompts within each class, thereby robustly aggregating multiple diagnostic criteria.

To ensure the validity of the comparisons, the proposed head, which incorporates feature map up-sampling and adaptive average pooling for downstream tasks, was employed for all CLIP variants. Furthermore, all competitive methods utilize their own segmentation or classification heads to ensure a fair comparison. It is imperative to acknowledge that LN-EXT is exclusively utilized for evaluation purposes; consequently, the test results for LN-EXT are derived directly from the model that was trained using LN-INT.

D. Segmentation Results

The quantitative segmentation results are presented in Table II. It is evident that the proposed HT strategy consistently enhances performance across all datasets and CLIP variants. Notably, applying HT to the vanilla CLIP [11] yields substantial improvements, achieving the highest Dice scores on LN-EXT (78.62%), BUSI (81.19%), TN3K (81.42%), and Prostate (92.11%) datasets. Similarly, MetaCLIP (HT) demonstrates top-tier performance on LN-INT (80.66%) and DDTI (90.42%).

When comparing HT-adapted models to their unadapted baselines, the performance gains are significant. For instance, on the challenging LN-INT dataset, CLIP (HT) surpasses the vanilla CLIP [11] by 9.62% in Dice score (80.55% vs. 70.93%), and MetaCLIP (HT) improves upon MetaCLIP [32] by 10.48% (80.66% vs. 70.18%). This trend of improvement is consistent across all metrics (IoU, HD95, ASD), with HT models exhibiting sharper boundary delineation as evidenced by lower HD95 and ASD scores. These findings indicate that HT can learn robust, transferable ultrasound representations even on small datasets.

Three CLIP variants were evaluated: BiomedCLIP [18], UniMedCLIP [19], and MetaCLIP [32]. While trained on large-scale internet and medical data, none of these domain-specific models in their original form consistently surpass or match the performance of HT-enhanced models and CLIPSeg [28]. We

attribute this to the modality gap: although trained on general and confounding medical image-text data, their representations may not generalize directly to the heterogeneous acoustic signatures of ultrasound without specific adaptation. However, when equipped with the HT adapter, these models show significant performance boosts, validating the effectiveness of the proposed method.

We randomly selected three samples per test set of the six datasets for visualization, as shown in Fig. 4. A thorough examination reveals that the proposed HT adaptation technique exhibits superior performance compared to other methods across all datasets, especially on the TN3K [23] and Prostate [24] datasets where it accurately delineates complex boundaries of thyroid nodule and prostate compares to baselines. These visual results align with the quantitative analysis.

Models equipped with HT demonstrated a marked improvement over the baselines, as evidenced by the second and third samples in the external test set (LN-EXT). The employment of HT models in depicting anatomical regions is characterized by a tendency to incorporate comprehensive and holistic approaches. This tendency is manifested through the strategic filling of internal voids and the refinement of lesion boundaries, thereby facilitating a more comprehensive depiction of the anatomical structure. Furthermore, although HT increases false positives (green area) while optimizing the true positives (yellow area) in the second sample from the BUSI [21] dataset, a divergent behavior is observed in other samples. This phenomenon is most evident in the last sample from the DDTI [22], the first sample from the TN3K [23], and the Prostate [24] datasets. The utilization of HT has been demonstrated to be a highly effective method for eliminating false positives in a substantial proportion of samples.

Finally, as demonstrated in Table II and Fig. 4, DINOV2 [13] exhibited the poorest performance, even comparing to the lightweight UNet. Despite being trained on a massive dataset (142 million images), it may lack the dense semantic support from text during pre-training. Consequently, it struggles with the domain gap between natural and medical ultrasound imaging data, leading to high false positive rates (*e.g.*, in TN3K [23] and Prostate [24] datasets) and notable uncertainties in prediction.

E. Classification Results

In this study, we evaluated a range of CLIP-based models and the HT strategy on three ultrasound classification datasets (LN-INT, LN-EXT, and BUSI [21]) as only they were labeled with diagnostic classes (*i.e.*, benign and malignant) according to the confirmed pathology results. The quantitative results for the zero-shot and supervised classification are illustrated in Table III.

Across all datasets, zero-shot results of vanilla and variants of CLIPs with adapters demonstrated classification accuracies that exhibited a high degree of consistency and were only marginally above random guessing, with AUC scores hovering near 50%. These results indicate that, in the absence of supervised fine-tuning on domain-specific ultrasound images, the pre-trained representations of CLIPs are inadequate to

TABLE II

SEGMENTATION RESULTS ON SIX ULTRASOUND DATASETS, AVERAGED OVER THREE RUNS WITH DIFFERENT RANDOM SEEDS. (HT) DENOTES HYBRID-TUNED MODELS. PERFORMANCE IMPROVEMENTS OVER BASELINES ARE HIGHLIGHTED.

Method	Params	LN-INT				LN-EXT				BUSI			
		Dice	IoU	HD95	ASD	Dice	IoU	HD95	ASD	Dice	IoU	HD95	ASD
UNet	1.8 M	77.41	68.36	24.99	9.03	70.54	59.82	34.08	11.25	76.97	67.11	26.42	8.45
CLIPSeg	1.1 M	73.14	62.31	26.58	10.16	73.28	62.61	28.44	9.88	79.35	69.24	19.47	6.65
DINOv2	9.7 M	62.09	49.51	140.41	52.31	56.54	43.26	147.87	59.19	61.29	48.28	177.75	72.43
CLIP	3.0 M	70.93	58.79	35.01	12.20	71.34	58.42	37.14	12.66	77.31	65.47	29.84	9.21
CLIP (HT)	4.4 M	80.55	71.94	18.44	6.81	78.62	68.20	22.69	7.60	81.19	71.25	17.84	5.45
MetaCLIP	2.8 M	70.18	58.01	40.24	13.86	68.82	55.73	41.58	14.11	76.12	64.22	30.47	9.07
MetaCLIP (HT)	4.1 M	80.66	71.75	18.71	6.86	77.14	66.53	23.65	8.01	80.74	70.64	18.21	5.86
UniMedCLIP	2.8 M	73.05	62.35	32.33	11.17	68.68	56.53	34.69	11.95	75.33	63.52	26.72	8.73
UniMedCLIP (HT)	4.1 M	78.85	70.17	18.89	6.63	75.22	64.39	25.53	8.63	78.85	68.37	20.08	6.44
BiomedCLIP	2.8 M	71.27	60.25	34.41	11.49	68.07	55.95	34.72	11.63	76.57	64.98	29.35	9.85
BiomedCLIP (HT)	4.1 M	79.45	70.31	20.81	7.40	74.46	63.84	25.16	8.46	79.73	69.29	21.78	7.05
Method	Params	DDTI				TN3K				Prostate			
		Dice	IoU	HD95	ASD	Dice	IoU	HD95	ASD	Dice	IoU	HD95	ASD
UNet	1.8 M	86.44	76.93	21.11	7.63	79.49	70.29	24.21	7.97	91.64	86.93	14.27	4.28
CLIPSeg	1.1 M	87.89	78.82	18.29	7.15	77.19	67.06	23.16	7.84	91.32	86.05	14.90	4.73
DINOv2	9.7 M	86.20	76.21	54.93	21.80	60.71	47.62	124.10	47.74	87.52	80.05	85.79	28.81
CLIP	3.0 M	87.56	78.32	19.63	7.66	72.89	61.22	36.32	12.09	90.53	84.56	23.41	7.18
CLIP (HT)	4.4 M	90.11	82.39	15.39	5.80	81.42	71.81	18.65	6.09	92.11	87.34	11.67	3.87
MetaCLIP	2.8 M	88.16	79.22	19.71	7.40	71.19	59.40	40.43	13.71	89.92	83.53	26.97	8.20
MetaCLIP (HT)	4.1 M	90.42	82.87	14.35	5.59	81.09	71.40	18.64	6.11	92.05	87.15	12.23	4.03
UniMedCLIP	2.8 M	88.73	80.11	18.00	6.72	71.51	59.80	34.95	12.10	90.36	84.43	18.88	6.01
UniMedCLIP (HT)	4.1 M	89.91	82.06	15.65	5.86	79.30	69.22	21.13	6.89	91.54	86.32	12.96	4.40
BiomedCLIP	2.8 M	88.55	79.85	18.49	6.90	72.76	61.05	34.37	11.45	90.87	84.85	19.48	6.09
BiomedCLIP (HT)	4.1 M	89.42	81.27	15.94	6.15	79.77	69.74	20.57	7.04	91.78	86.75	12.62	4.23

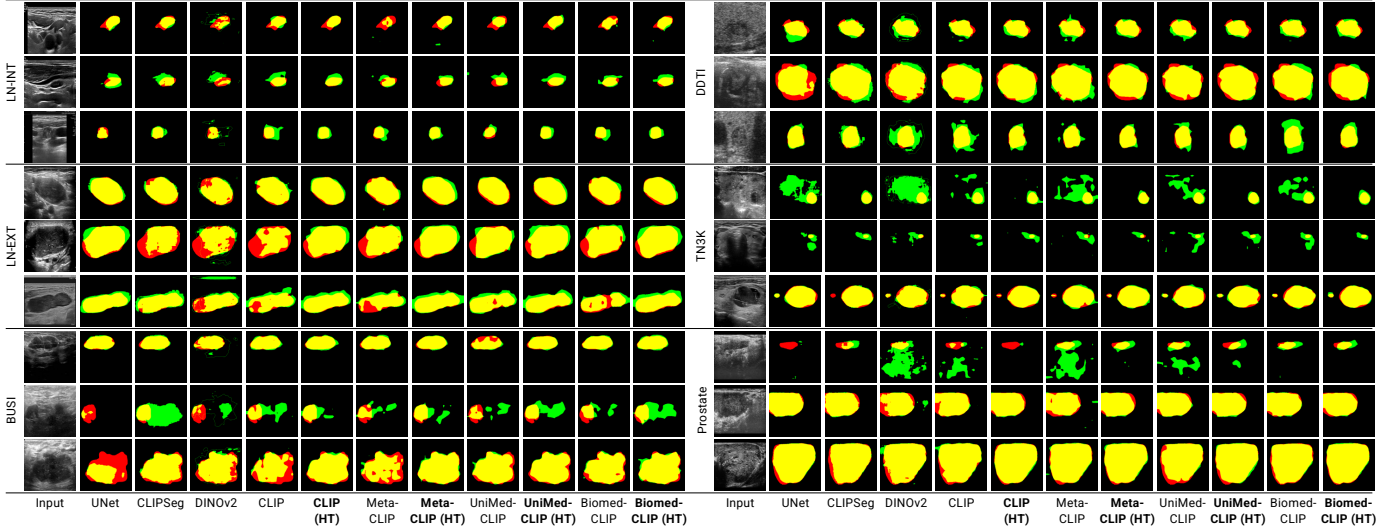


Fig. 4. Segmentation visualization on LN-INT, LN-EXT, BUSI [21], DDTI [22], TN3K [23], and Prostate [24] datasets. The first column shows the input images. Regions in red, green and yellow indicate the ground truth, false positive and true positive, respectively. Hybrid-tuned models are in bold.

support clinically meaningful classification. Although the HT model has been demonstrated to enhance the efficacy of zero-shot classification for CLIP [11] in the LN-EXT dataset, with marginal improvements of 8.04% and 6.73% in accuracy and AUC, respectively, it is important to note that other HT models exhibit a decline in performance when compared to their baselines. This pattern suggests that small-scale fine-tuning may compromise the delicate feature distribution of CLIPs and precipitate catastrophic forgetting. Therefore, the implementation of meticulously engineered tuning techniques is imperative to ensure the efficacy of the process.

For the supervised classification task, the proposed HT

strategy demonstrates a consistent performance improvement across various CLIP-based models. As presented in Table III, UniMedCLIP (HT) achieves the highest performance among CLIP variants, with an average accuracy of 83.05% and an AUC of 91.44%, surpassing the vanilla UniMedCLIP [19]. Notably, BiomedCLIP (HT) also shows significant gains, improving the average accuracy and AUC by 3.75% and 3.55%, respectively, compared to its baseline. These results highlight the capability of HT to effectively adapt general medical vision-language models to the ultrasound domain.

In comparison with traditional deep learning models, ResNet18 [40] achieves a competitive average accuracy of

TABLE III

CLASSIFICATION RESULTS ON THREE ULTRASOUND DATASETS, AVERAGED OVER THREE RUNS WITH DIFFERENT RANDOM SEEDS. (HT) DENOTES HYBRID-TUNED MODELS. PERFORMANCE IMPROVEMENTS OVER BASELINES ARE HIGHLIGHTED.

	Method	Params	LN-INT		LN-EXT		BUSI		Average	
			Acc	AUC	Acc	AUC	Acc	AUC	Acc	AUC
Zero-shot	CLIP	3.0 M	61.19	58.39	54.55	71.75	70.48	69.96	62.07	66.70
	CLIP (HT)	4.4 M	44.02	63.78	62.48	78.48	35.50	58.21	47.33	66.82
	MetaCLIP	2.8 M	57.19	57.10	56.68	61.43	62.60	59.24	58.82	59.26
	MetaCLIP (HT)	4.1 M	41.50	47.62	39.04	37.06	47.55	53.54	42.70	46.07
	UniMedCLIP	2.8 M	47.50	47.83	43.76	37.34	56.15	53.04	49.14	46.07
	UniMedCLIP (HT)	4.1 M	40.09	45.14	46.61	41.22	36.07	56.22	40.92	47.53
	BiomedCLIP	2.8 M	58.68	61.42	63.64	64.75	52.24	70.59	58.19	65.59
	BiomedCLIP (HT)	4.1 M	40.48	56.74	50.18	50.22	44.51	63.30	45.06	56.75
	ResNet18	11.2 M	87.40	94.94	74.69	87.32	90.62	95.45	84.24	92.57
Supervised	DINOv2	7.7 K	57.48	66.82	51.16	69.72	64.06	64.27	57.57	66.94
	CLIP	3.0 M	86.61	92.21	74.78	83.88	82.29	90.94	81.23	89.01
	CLIP (HT)	4.4 M	86.61	92.34	74.33	87.21	82.81	90.17	81.25	89.91
	MetaCLIP	2.8 M	84.25	91.59	74.69	88.57	82.29	90.66	80.41	90.28
	MetaCLIP (HT)	4.1 M	85.57	92.79	76.56	86.85	82.81	85.52	81.65	88.39
	UniMedCLIP	2.8 M	83.46	92.03	75.13	84.86	84.38	94.86	80.99	90.58
	UniMedCLIP (HT)	4.1 M	85.56	93.59	74.51	87.26	89.06	93.47	83.05	91.44
	BiomedCLIP	2.8 M	84.52	91.95	65.42	76.99	81.25	90.83	77.06	86.59
	BiomedCLIP (HT)	4.1 M	86.61	93.06	69.87	85.52	85.94	91.84	80.81	90.14

84.24%. However, it is important to note that ResNet18 involves a large number of parameters that need to be trained. In contrast, the HT strategy allows CLIP variants to achieve comparable performance (e.g., UniMedCLIP (HT) vs. ResNet18) with significantly fewer trainable parameters (*i.e.*, 4.1 M vs. 11.2 M), demonstrating superior parameter efficiency. On the other hand, DINOv2 [13] exhibits suboptimal performance with an average accuracy of 57.57%, which is considerably lower than both ResNet18 and the HT-enhanced CLIP models. This disparity further emphasizes the advantage of the proposed method in efficiently leveraging pre-trained representations for downstream tasks.

F. Few-shot Results

To investigate the data efficiency of the proposed method, a series of few-shot learning experiments were conducted on both segmentation and classification tasks. The training data ratio varies from 1% to 50% and the performance of BiomedCLIP [18] and its adaptation variants (LoRA [33] and the proposed HT) are compared. The quantitative outcomes and the segmentation visualizations are presented in Table IV and Fig. 5, respectively.

In terms of segmentation, the HT strategy demonstrates superior data efficiency and performance stability. Even with extremely limited data (1% ratio), HT achieves competitive Dice scores (63.55%) compared to the baseline BiomedCLIP [18] (63.98%) while significantly outperforming it in boundary metrics (HD95: 39.05 vs. 41.18; ASD: 14.64 vs. 15.58). As the training data ratio increases, the advantage of HT becomes more pronounced. From 2% to 50% ratios, HT consistently achieves the best performance across all segmentation metrics. For instance, at 20% ratio, HT surpasses BiomedCLIP by 3.29% in Dice and reduces HD95 by 8.37, indicating that the HT module effectively captures detailed anatomical structures and boundaries with limited supervision. Furthermore, HT consistently outperforms LoRA [33], suggesting that the hybrid

TABLE IV
FEW-SHOT SEGMENTATION AND CLASSIFICATION RESULTS ON ALL AVAILABLE DATASETS, AVERAGED OVER THREE RUNS WITH DIFFERENT RANDOM SEEDS. LORA AND HT DENOTE LORA-TUNED AND HYBRID-TUNED MODELS. RATIO REPRESENTS THE PROPORTION OF TOTAL DATA USED FOR TRAINING. THE **BEST** RESULTS ARE HIGHLIGHTED.

Ratio	Method	Segmentation Average				Classification Average			
		Dice	IoU	HD95	ASD	Acc	Rec	Pre	F1
1%	BiomedCLIP	63.98	51.64	41.18	15.58	60.60	21.46	57.78	30.74
	LoRA	58.01	45.97	41.08	15.12	56.14	6.88	63.64	10.62
	HT	63.55	51.73	39.05	14.64	59.26	23.06	68.55	32.93
2%	BiomedCLIP	67.37	55.30	38.02	14.31	67.85	35.22	75.64	44.95
	LoRA	62.28	50.06	41.51	15.35	65.44	37.63	67.19	46.16
	HT	68.36	56.91	34.50	12.79	67.45	31.89	71.94	42.07
5%	BiomedCLIP	69.82	58.38	34.06	12.54	68.35	46.16	73.80	56.11
	LoRA	65.98	53.41	40.29	14.85	66.34	61.12	72.13	58.37
	HT	71.73	60.81	29.51	10.75	65.09	35.09	46.71	39.52
10%	BiomedCLIP	72.37	61.17	33.12	11.85	73.09	58.67	75.65	64.82
	LoRA	65.97	53.14	41.00	15.32	66.02	25.61	93.81	34.89
	HT	74.68	64.10	27.30	9.81	73.63	51.83	80.98	62.11
20%	BiomedCLIP	74.18	63.34	32.48	11.42	74.62	54.03	82.03	63.84
	LoRA	66.94	54.09	43.54	16.43	70.35	39.66	85.13	49.72
	HT	77.47	67.48	24.11	8.52	76.12	58.49	81.02	67.18
35%	BiomedCLIP	75.42	64.77	30.68	10.60	75.69	56.15	83.05	66.26
	LoRA	66.37	53.59	44.00	16.73	73.65	56.20	81.72	62.12
	HT	78.94	69.28	22.24	7.83	76.76	58.86	83.44	67.83
50%	BiomedCLIP	76.55	66.03	29.48	10.30	75.69	55.52	83.47	65.89
	LoRA	66.88	54.01	46.26	17.42	69.47	33.15	92.37	42.85
	HT	80.27	70.81	21.61	7.54	77.16	57.54	86.60	68.02

tuning strategy is more effective than standard parameter-efficient fine-tuning (PEFT) for dense prediction tasks in ultrasound.

For classification, the HT model also exhibits robust performance. At the 1% ratio, HT achieves the highest AUC (65.27%) and F1 score (32.93%), demonstrating its capability to learn discriminative features from scarce data. While the performance fluctuates slightly at lower ratios (2%-5%), HT establishes a clear lead as the data volume increases. At 20%, 35%, and 50% ratios, it consistently secures the highest Accuracy, Recall, F1, and AUC scores. Notably, at the 50% ratio, HT

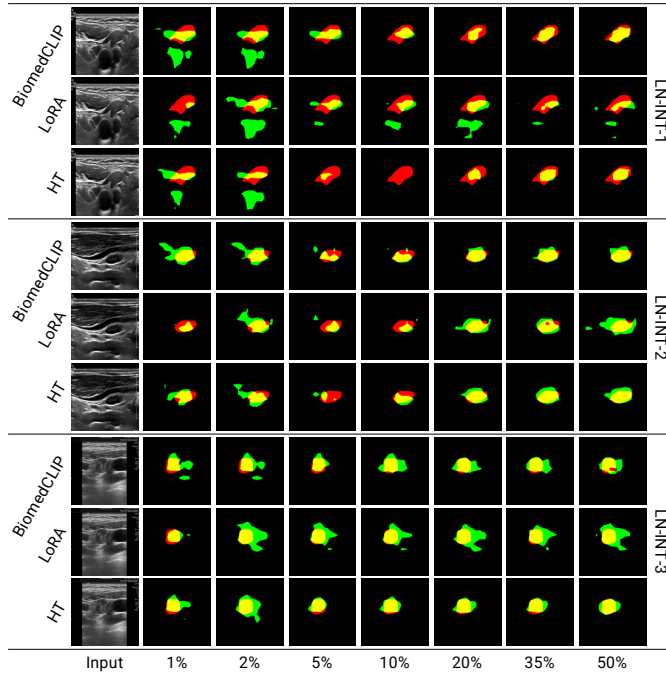


Fig. 5. Few-shot segmentation visualization on LN-INT dataset. The first column shows the input images. The percentages represent the amount of data used for model training. Regions in red, green and yellow indicate the ground truth, false positive and true positive, respectively.

achieves an accuracy of 77.16% and an AUC of 86.51%, significantly outperforming both the baseline BiomedCLIP [18] and LoRA [33]. This trend confirms that the HT strategy not only adapts well to the domain but also scales effectively with available data, mitigating the risk of over-fitting or catastrophic forgetting often observed in zero-shot and few-shot scenarios.

G. Ablation Studies

To verify the effectiveness of the proposed method, we conducted comprehensive ablation studies on segmentation, classification, and the internal components of the HT module based on BiomedCLIP [18].

Effectiveness on Segmentation. We first evaluate the impact of different tuning strategies on segmentation performance, as reported in Table V. The proposed HT method achieves the highest average Dice score of 82.44% and IoU of 73.53%, consistently outperforming other approaches. A notable observation is the performance of LoRA-based methods. Despite being a popular PEFT technique, LoRA [33] exhibits a significant performance degradation compared to the baseline (e.g., Average Dice: 66.37% vs. 78.02%). Even when fine-tuning both visual and text encoders (LoRA V+T) to align the modalities, the performance remains suboptimal (66.64%). This suggests that modifying the internal weights of the pre-trained encoders on limited ultrasound data may disrupt the learned general medical representations, leading to negative transfer. In contrast, adapter-based methods like Mona [34] and HT, which freeze the backbone and learn additional adaptation layers, effectively preserve the pre-trained knowledge while adapting to the specific domain, resulting in superior segmentation accuracy.

TABLE V
ABLATION STUDIES OF DIFFERENT ADAPTERS FOR SUPERVISED SEGMENTATION, AVERAGED OVER THREE RUNS WITH DIFFERENT RANDOM SEEDS. THE **BEST** AND **SECOND BEST** RESULTS ARE HIGHLIGHTED.

	Method	Dice	IoU	HD95	ASD
LN-INT	Baseline	71.27	60.25	34.41	11.49
	LoRA (V+T)	56.67	42.87	55.69	21.41
	LoRA	56.75	43.01	56.30	22.10
	Mona	79.05	69.77	20.80	7.59
	HT	79.45	70.31	20.81	7.40
LN-EXT	Baseline	68.07	55.95	34.72	11.63
	LoRA (V+T)	61.83	48.38	49.41	17.80
	LoRA	61.51	48.21	49.94	18.48
	Mona	74.56	63.73	25.22	8.38
	HT	74.46	63.84	25.16	8.46
BUSI	Baseline	65.57	64.98	29.35	9.85
	LoRA (V+T)	62.34	49.23	46.03	16.49
	LoRA	63.28	49.68	45.44	15.89
	Mona	79.40	68.89	21.40	7.06
	HT	79.73	69.29	21.78	7.05
DDTI	Baseline	88.55	79.85	18.49	6.90
	LoRA (V+T)	81.26	69.58	28.76	11.06
	LoRA	81.40	69.57	28.04	11.02
	Mona	89.50	81.44	16.33	6.20
	HT	89.42	81.27	15.94	6.15
TN3K	Baseline	72.76	61.05	34.37	11.45
	LoRA (V+T)	57.71	44.59	67.05	26.21
	LoRA	55.34	42.32	72.94	29.17
	Mona	79.84	69.78	19.97	6.81
	HT	79.77	69.74	20.57	7.04
Prostate	Baseline	90.87	84.85	19.48	6.09
	LoRA (V+T)	80.05	68.48	41.76	15.21
	LoRA	79.95	68.29	41.67	15.50
	Mona	91.56	86.47	12.65	4.21
	HT	91.78	86.75	12.62	4.23
Average	Baseline	78.02	67.82	28.47	9.57
	LoRA (V+T)	66.64	53.85	48.12	18.03
	LoRA	66.37	53.51	49.06	18.69
	Mona	82.32	73.35	19.40	6.71
	HT	82.44	73.53	19.48	6.72

Effectiveness on Classification. A similar trend is observed in the classification task, as shown in Table VI. The HT strategy secures the top performance with an average accuracy of 80.81% and an AUC of 90.14%. While the Mona [34] adapter also improves over the baseline (78.84% vs. 77.06%), the LoRA [33] variants again fail to yield positive gains. Specifically, LoRA and LoRA (V+T) result in average accuracies of 68.92% and 70.17%, respectively, both falling below the baseline. This consistent underperformance of LoRA across tasks further confirms that preserving the integrity of the pre-trained backbone is crucial for small-scale ultrasound datasets. The HT strategy successfully bridges the domain gap without compromising the robust feature extraction capabilities of the original model.

Component Analysis of HT Module. Finally, we analyze the contribution of individual components within the HT module: the Noise Estimation (NE) and Frequency Filtering (FF) blocks. As presented in Table VII, we compare the full HT model with variants using only NE or FF, as well as the Mona [34] adapter. The results demonstrate that both components contribute to the overall performance. The Full HT model achieves the best results in both segmentation and classification. Notably, the NE module appears to play a pivotal role; using NE alone yields an average classification accuracy

TABLE VI

ABLATION STUDIES OF DIFFERENT ADAPTERS FOR SUPERVISED CLASSIFICATION, AVERAGED OVER THREE RUNS WITH DIFFERENT RANDOM SEEDS. THE **BEST** AND **SECOND BEST** RESULTS ARE HIGHLIGHTED.

	Method	Acc	Rec	Pre	F1	AUC
LN-INT	Baseline	84.52	79.01	83.66	81.23	91.95
	LoRA (V+T)	64.30	53.09	69.08	50.26	78.20
	LoRA	62.73	14.81	75.06	23.27	81.30
	Mona	83.20	72.84	85.58	78.67	93.27
	HT	86.61	80.25	87.33	83.60	93.06
LN-EXT	Baseline	65.42	37.86	82.40	51.80	76.99
	LoRA (V+T)	71.21	69.57	80.39	66.85	87.86
	LoRA	71.12	42.21	98.48	54.92	91.02
	Mona	67.38	38.95	88.44	54.02	84.43
	HT	69.87	44.38	88.84	59.07	85.52
BUSI	Baseline	81.25	63.89	82.07	71.84	90.83
	LoRA (V+T)	75.00	51.39	86.87	57.11	83.44
	LoRA	72.91	27.78	100.0	40.04	82.98
	Mona	85.94	69.45	90.71	78.57	92.85
	HT	85.94	68.06	92.62	78.29	91.84
Average	Baseline	77.06	60.25	82.70	68.29	86.59
	LoRA (V+T)	70.17	58.01	78.78	58.08	83.17
	LoRA	68.92	28.27	91.18	39.41	85.10
	Mona	78.84	60.41	88.24	70.42	90.18
	HT	80.81	64.23	89.60	73.65	90.14

of 80.38%, which is higher than using FF alone (79.51%) and Mona (78.84%). This indicates that estimating and mitigating the noise or uncertainty in the pre-trained features is essential for robust ultrasound image analysis. The combination of NE and FF (Full) further enhances the performance, validating the synergistic effect of the proposed hybrid tuning architecture.

TABLE VII

ABLATION STUDIES OF DIFFERENT ADAPTER MODULES FOR SUPERVISED SEGMENTATION AND CLASSIFICATION, AVERAGED OVER THREE RUNS WITH DIFFERENT RANDOM SEEDS. THE **BEST** AND **SECOND BEST** RESULTS ARE HIGHLIGHTED.

Method	Segmentation Average			Classification Average					
	Dice	IoU	HD95	ASD	Acc	Rec	Pre	F1	AUC
Mona	82.32	73.35	19.40	6.71	78.84	60.41	88.24	70.42	90.18
HT (NE only)	82.43	73.53	19.42	6.71	80.38	62.96	90.17	72.38	89.94
HT (FF only)	82.32	73.37	19.33	6.70	79.51	62.01	88.50	71.52	90.52
HT (Full)	82.44	73.53	19.48	6.72	80.81	64.23	89.60	73.65	90.14

H. Limitation and Future Perspectives

Despite the effectiveness of the proposed HT strategy, three limitations necessitate further investigation.

First, backbone networks such as BiomedCLIP [18] are pre-trained on biomedical or natural data. These multimodal biomedical datasets encompass diverse sources, including pathological images and text, CT and MRI scans and reports, *etc*. In contrast, ultrasound data comprises a relatively small proportion of these datasets and are often of poor quality. Therefore, pre-trained models frequently demonstrate deficiencies in their native encoding of ultrasound characteristics, including speckle noise and shadowing from images and terminologies in the textual context. Consequently, the availability of a large-scale high-quality multimodal ultrasound dataset in a CoCo [41], [42] style is critical for the advancement of vision-language development in ultrasound.

Second, despite employing clinically detailed prompts, the model struggles to map these high-level semantic concepts to low-level ultrasound acoustic patterns without explicit supervision. This suggests that the pre-trained visual encoder lacks the specific sensitivity to sonographic features required for zero-shot reasoning. Future work could explore test-time adaptation to dynamically calibrate feature distributions during inference, or retrieval-augmented classification to ground diagnostic decisions in a reference database of confirmed cases.

Third, the failure of joint fine-tuning (*e.g.*, LoRA V+T) indicates a misalignment between global CLIP representations and fine-grained diagnostic criteria. Current methods primarily refine visual features, potentially under-utilizing clinical textual knowledge. To achieve a more effective integration of images and text in ultrasound, it is imperative to explore the implementation of a learnable context optimization technique or a robust textual adaptation method.

V. CONCLUSION

We presented a novel Hybrid-tuning (HT) strategy to effectively adapt general VLMs for medical ultrasound analysis. Addressing the unique challenges of ultrasound imaging, our HT module integrates frequency-domain filtering and dynamic noise estimation directly into the frozen visual backbone. Extensive experiments across six diverse datasets (including Lymph Node, Breast, Thyroid, and Prostate) demonstrate that HT significantly outperforms existing SOTA methods, including standard fine-tuning (LoRA) and domain-specific VLMs (BiomedCLIP), in both segmentation and classification tasks. Notably, our approach exhibits remarkable data efficiency, achieving robust performance in few-shot scenarios where labeled data is scarce. While zero-shot generalization remains a challenge due to the profound modality gap, our findings confirm that parameter-efficient transfer learning is a viable path toward foundational ultrasound intelligence. Future work will focus on enhancing cross-modal alignment and exploring test-time adaptation to further bridge the divide between natural and sonographic vision.

VI. ACKNOWLEDGEMENT

This work was supported by General Research Funds of the Research Grant Council of Hong Kong (Reference no. 15102222 and 15102524).

REFERENCES

- [1] R. F. Brem, M. J. Lenihan, J. Lieberman, and J. Torrente, “Screening breast ultrasound: Past, present, and future,” *American Journal of Roentgenology*, vol. 204, no. 2, pp. 234–240, 2015.
- [2] S. Takashima, H. Fukuda, N. Nomura, H. Kishimoto, T. Kim, and T. Kobayashi, “Thyroid nodules: Re-evaluation with ultrasound,” *Journal of Clinical Ultrasound*, vol. 23, no. 3, pp. 179–184, 1995.
- [3] M. Ying and A. Ahuja, “Sonography of neck lymph nodes. part i: Normal lymph nodes,” *Clinical Radiology*, vol. 58, no. 5, pp. 351–358, 2003.
- [4] A. T. Ahuja and M. Ying, “Sonographic evaluation of cervical lymph nodes,” *American Journal of Roentgenology*, vol. 184, no. 5, pp. 1691–1699, 2005.
- [5] A. T. Ahuja, M. Ying, S. Y. Ho, G. Antonio, Y. P. Lee, A. D. King, and K. T. Wong, “Ultrasound of malignant cervical lymph nodes,” *Cancer Imaging*, vol. 8, no. 1, pp. 48–56, 2008.

[6] X. Han, J. Qu, M.-L. Chui, S. T. Gunda, Z. Chen, J. Qin, A. D. King, W. C.-W. Chu, J. Cai, and M. T.-C. Ying, "Artificial intelligence performance in ultrasound-based lymph node diagnosis: a systematic review and meta-analysis," *BMC cancer*, vol. 25, no. 1, p. 73, 2025.

[7] M. X. Han, M. T.-C. Ying, M. J. Qu, Z. Chen, M. S. T. Gunda, J. Cai, J. Qin, W. C. W. Chu, and A. D. King, "Differentiation of benign and malignant lymph nodes using ultrasound-based radiomics and machine learning," *Journal of Medical Imaging and Radiation Sciences*, vol. 55, no. 3, p. 101544, 2024.

[8] O. Ronneberger, P. Fischer, and T. Brox, "U-net: Convolutional networks for biomedical image segmentation," in *Medical image computing and computer-assisted intervention-MICCAI 2015: 18th international conference, Munich, Germany, October 5-9, 2015, proceedings, part III* 18. Springer, 2015, Conference Proceedings, pp. 234–241.

[9] J. Qu, X. Han, M.-L. Chui, Y. Pu, S. T. Gunda, Z. Chen, J. Qin, A. D. King, W. C.-W. Chu, J. Cai, and M. T.-C. Ying, "The application of deep learning for lymph node segmentation: A systematic review," *IEEE Access*, vol. 13, pp. 97208–97227, 2025.

[10] R. Bommasani, D. A. Hudson, E. Adeli, R. Altman, S. Arora, S. von Arx, M. S. Bernstein, J. Bohg, A. Bosselut, E. Brunskill *et al.*, "On the opportunities and risks of foundation models," *arXiv:2108.07258*, 2021.

[11] A. Radford, J. W. Kim, C. Hallacy, A. Ramesh, G. Goh, S. Agarwal, G. Sastry, A. Askell, P. Mishkin, J. Clark *et al.*, "Learning transferable visual models from natural language supervision," in *International conference on machine learning*. PMLR, 2021, pp. 8748–8763.

[12] A. Kirillov, E. Mintun, N. Ravi, H. Mao, C. Rolland, L. Gustafson, T. Xiao, S. Whitehead, A. C. Berg, W.-Y. Lo, P. Dollár, and R. Girshick, "Segment anything," *arXiv:2304.02643*, 2023.

[13] M. Oquab, T. Darcot, T. Moutakanni, H. Vo, M. Szafraniec, V. Khalidov, P. Fernandez, D. Haziza, F. Massa, A. El-Nouby *et al.*, "Dinov2: Learning robust visual features without supervision," *arXiv:2304.07193*, 2023.

[14] J. Wang, D. Chen, Z. Wu, C. Luo, L. Zhou, Y. Zhao, Y. Xie, C. Liu, Y.-G. Jiang, and L. Yuan, "Omnivl: One foundation model for image-language and video-language tasks," *Advances in neural information processing systems*, vol. 35, pp. 5696–5710, 2022.

[15] J. Jiao, J. Zhou, X. Li, M. Xia, Y. Huang, L. Huang, N. Wang, X. Zhang, S. Zhou, Y. Wang *et al.*, "Usfm: A universal ultrasound foundation model generalized to tasks and organs towards label efficient image analysis," *Medical Image Analysis*, vol. 96, p. 103202, 2024.

[16] A. Meyer, A. Murali, D. Mutter, and N. Padov, "Ultrasam: A foundation model for ultrasound using large open-access segmentation datasets," *arXiv:2411.16222*, 2024.

[17] K. Poudel, M. Dhakal, P. Bhandari, R. Adhikari, S. Thapaliya, and B. Khanal, "Exploring transfer learning in medical image segmentation using vision-language models," in *International Conference on Medical Imaging with Deep Learning*, 2023.

[18] S. Zhang, Y. Xu, N. Usuyama, H. Xu, J. Bagga, R. Tinn, S. Preston, R. Rao, M. Wei, N. Valluri *et al.*, "Biomedclip: a multimodal biomedical foundation model pretrained from fifteen million scientific image-text pairs," *arXiv preprint arXiv:2303.00915*, 2023.

[19] M. U. Khattak, S. Kunhimon, M. Naseer, S. Khan, and F. S. Khan, "Unimed-clip: Towards a unified image-text pretraining paradigm for diverse medical imaging modalities," *arXiv preprint arXiv:2412.10372*, 2024.

[20] Z. Wang, Z. Wu, D. Agarwal, and J. Sun, "Medclip: Contrastive learning from unpaired medical images and text," *Proceedings of the Conference on Empirical Methods in Natural Language Processing. Conference on Empirical Methods in Natural Language Processing*, vol. 2022, pp. 3876–3887, 2022.

[21] W. Al-Dhabyani, M. Gomaa, H. Khaled, and A. Fahmy, "Dataset of breast ultrasound images," *Data in Brief*, vol. 28, p. 104863, 2020.

[22] L. Pedraza, C. Vargas, F. Narváez, O. Durán, E. Muñoz, and E. Romero, *An open access thyroid ultrasound image database*, ser. Tenth International Symposium on Medical Information Processing and Analysis. SPIE, 2015, vol. 9287.

[23] H. Gong, J. Chen, G. Chen, H. Li, G. Li, and F. Chen, "Thyroid region prior guided attention for ultrasound segmentation of thyroid nodules," *Computers in Biology and Medicine*, vol. 155, p. 106389, 2023.

[24] H. Jiang, M. Imran, P. Muralidharan, A. Patel, J. Pensa, M. Liang, T. Benidir, J. R. Grajo, J. P. Joseph, R. S. Terry, J. M. DiBianco, L. Su, Y. Zhou, W. Brisbane, and W. Shao, "Microsegnet: A deep learning approach for prostate segmentation on micro-ultrasound images," *Computerized medical imaging and graphics : the official journal of the Computerized Medical Imaging Society*, vol. 112, p. 102326, 2023.

[25] A. Radford, K. Narasimhan, T. Salimans, I. Sutskever *et al.*, "Improving language understanding by generative pre-training," 2018.

[26] J. Devlin, M.-W. Chang, K. Lee, and K. Toutanova, "Bert: Pre-training of deep bidirectional transformers for language understanding," in *North American Chapter of the Association for Computational Linguistics*, 2019.

[27] S. Eslami, G. de Melo, and C. Meinel, "Does clip benefit visual question answering in the medical domain as much as it does in the general domain?" *ArXiv*, vol. abs/2112.13906, 2021.

[28] T. Lüddecke and A. Ecker, "Image segmentation using text and image prompts," in *Proceedings of the IEEE/CVF conference on computer vision and pattern recognition*, 2022, pp. 7086–7096.

[29] J. P. Huix, A. R. Ganeshan, J. F. Haslum, M. Söderberg, C. Matsoukas, and K. Smith, "Are natural domain foundation models useful for medical image classification?" in *Proceedings of the IEEE/CVF winter conference on applications of computer vision*, 2024, pp. 7634–7643.

[30] J. Deng, W. Dong, R. Socher, L.-J. Li, K. Li, and L. Fei-Fei, "Imagenet: A large-scale hierarchical image database," in *2009 IEEE conference on computer vision and pattern recognition*. Ieee, 2009, pp. 248–255.

[31] W. Lin, Z. Zhao, X. Zhang, C. Wu, Y. Zhang, Y. Wang, and W. Xie, "Pmc-clip: Contrastive language-image pre-training using biomedical documents," in *International Conference on Medical Image Computing and Computer-Assisted Intervention*. Springer, 2023, pp. 525–536.

[32] H. Xu, S. Xie, X. E. Tan, P.-Y. Huang, R. Howes, V. Sharma, S.-W. Li, G. Ghosh, L. Zettlemoyer, and C. Feichtenhofer, "Demystifying clip data," *arXiv preprint arXiv:2309.16671*, 2023.

[33] E. J. Hu, Y. Shen, P. Wallis, Z. Allen-Zhu, Y. Li, S. Wang, L. Wang, W. Chen *et al.*, "Lora: Low-rank adaptation of large language models," *ICLR*, vol. 1, no. 2, p. 3, 2022.

[34] D. Yin, L. Hu, B. Li, Y. Zhang, and X. Yang, "5% 100%: Breaking performance shackles of full fine-tuning on visual recognition tasks," *arXiv preprint arXiv:2408.08345*, 2024.

[35] Z. Liu, Y. Lin, Y. Cao, H. Hu, Y. Wei, Z. Zhang, S. Lin, and B. Guo, "Swin transformer: Hierarchical vision transformer using shifted windows," in *Proceedings of the IEEE/CVF international conference on computer vision*, 2021, pp. 10 012–10 022.

[36] A. Dosovitskiy, "An image is worth 16x16 words: Transformers for image recognition at scale," *arXiv preprint arXiv:2010.11929*, 2020.

[37] J. Li, T. Su, B. Zhao, F. Lv, Q. Wang, N. Navab, Y. Hu, and Z. Jiang, "Ultrasound report generation with cross-modality feature alignment via unsupervised guidance," *IEEE Transactions on Medical Imaging*, 2024.

[38] I. Siragusa, S. Contino, M. L. Ciura, R. Alicata, and R. Pirrone, "Medpix 2.0: A comprehensive multimodal biomedical data set for advanced ai applications with retrieval augmented generation and knowledge graphs," *Data Science and Engineering*, pp. 1–17, 2025.

[39] A. Yang, A. Li, B. Yang, B. Zhang, B. Hui, B. Zheng, B. Yu, C. Gao, C. Huang, C. Lv *et al.*, "Qwen3 technical report," *arXiv preprint arXiv:2505.09388*, 2025.

[40] K. He, X. Zhang, S. Ren, and J. Sun, "Deep residual learning for image recognition," in *Proceedings of the IEEE conference on computer vision and pattern recognition*, 2016, pp. 770–778.

[41] T.-Y. Lin, M. Maire, S. Belongie, J. Hays, P. Perona, D. Ramanan, P. Dollár, and C. L. Zitnick, "Microsoft coco: Common objects in context," in *European conference on computer vision*. Springer, 2014, pp. 740–755.

[42] J. Rückert, L. Bloch, R. Brüngel, A. Idrissi-Yaghir, H. Schäfer, C. S. Schmidt, S. Koitka, O. Pelka, A. B. Abacha, A. G. Seco de Herrera *et al.*, "Rocov2: Radiology objects in context version 2, an updated multimodal image dataset," *Scientific Data*, vol. 11, no. 1, p. 688, 2024.